Title
Density matrix model for polarons in a terahertz quantum dot cascade laser

Journal
Physical Review B, 90(15)

ISSN
2469-9950

Authors
Burnett, Benjamin A
Williams, Benjamin S

Publication Date
2014-10-01

DOI
10.1103/physrevb.90.155309

Peer reviewed

Density matrix model for polarons in a terahertz quantum dot cascade laser

Benjamin A. Burnett* and Benjamin S. Williams
Department of Electrical Engineering, University of California, Los Angeles, Los Angeles, California 90095, USA
(Received 25 July 2014; revised manuscript received 26 September 2014; published 16 October 2014)

A density matrix based method is introduced for computation of steady-state dynamics in quantum cascade systems of arbitrary size, which incorporates an optical field coherently. The method is applied to a model terahertz quantum dot cascade laser system, where a means of treating coherent electron-optical-phonon coupling is also introduced. Results predict a strong increase in the upper state lifetime and operating temperature as compared to traditional well-based terahertz quantum cascade lasers. However, new complications also arise, including multiple peaks in the gain spectrum due to strong electron-phonon coupling, and strong parasitic subthreshold current channels that arise due to reduced dephasing. It is anticipated that novel design schemes will be necessary for such lasers to become a reality.

DOI: 10.1103/PhysRevB.90.155309 PACS number(s): 42.70.Hj, 07.57.Hm, 73.63.Nm, 73.63.Kv

I. INTRODUCTION

Quantum cascade (QC) lasers based on intersubband transitions now cover large segments of the mid-infrared and terahertz spectral ranges [1–3]. However, because the quantum confinement is in only one dimension, electrons are free to move in-plane, and hence each subband supports a continuum of states above its minimum energy. This has a major impact on the electron dynamics, as it allows fast relaxation of electrons between subbands via the emission of longitudinal optical (LO) phonons, even when the intersubband energy separation is different from the LO phonon energy ($E_{LO} \approx 36$ meV in GaAs). This is particularly damaging for terahertz (THz) QC lasers, which have radiative energies less than E_{LO} ($\hbar\omega \sim$ 5–20 meV), and are still limited to cryogenic temperatures ($T_{max} = 200$ K) [4]. At low temperature, electrons reside near the upper subband minimum, and have insufficient energy to emit an LO- phonon. However, as the device warms, electrons gain sufficient in-plane energy to emit an LO phonon, which leads to an exponential decrease in the upper state lifetime to far subpicosecond levels at 300 K. This leads to a concomitant decrease in the population inversion with temperature, and is believed to be the primary inhibitor to room temperature operation [3,5].

It has been proposed by several authors that room temperature could be reached in THz QC lasers by introducing lateral quantum confinement so that the electronic density of states becomes fully discrete, i.e., sublevels instead of subbands [6–8]. In this way, it may be possible to greatly increase the upper radiative state lifetime if LO-phonon scattering can be suppressed across the radiative transition by intentional misalignment of all associated transitions from E_{LO}, utilizing an effect known as "phonon bottleneck." Candidate schemes include self-assembled quantum dots [9,10], quantum posts [11], and nanopillars etched from the top down into planar quantum-cascade material [12–14]. The concept of a phonon bottleneck for carrier relaxation has been shown to be of limited validity for interband devices (such as QD diode lasers), unless multiphonon, electron-electron, and electron-hole scattering processes are carefully prevented [15]. However, dramatic increases in intersublevel relaxation times have been observed experimentally where the relevant conditions are met; for unipolar self-assembled quantum dots with intersublevel energy separation less than E_{LO}, relaxation times as long as 1 ns were measured at 10 K, and many tens of picoseconds at room temperature [16].

A series of theoretical and experimental investigations on the electron-LO-phonon interaction in quantum dots has convincingly shown that the usual Fermi's "golden rule" approach is not appropriate given that there is not a continuum of final states. This suppresses decoherence so that the degenerate LO-phonon modes can form a strongly coupled system with the intersublevel excitation, leading to sustained Rabi oscillations and the formation of intersublevel polarons [17–21]. In isolated quantum dots, this persists until interruption by another interaction, likely the anharmonic decay of the LO phonon [22,23]. This picture dramatically modifies the energy-selectivity of the LO-phonon interaction, and introduces a complex series of anticrossed energy levels, leading to stark new features in transport characteristics and gain spectra which must be properly modeled if quantum-dot QC lasers are to be realized.

Candidate models must incorporate coherent electron-phonon interaction as well as coherent response to the optical field. The most detailed approach involves nonequilibrium Green's function (NEGF) methods, which provide motivation for the lateral confinement approach, but are extremely computationally intensive and also tedious for the nonexpert [24–29]. Density matrix models are attractive since they allow intuitive use of quantum-cascade wave functions as a basis and have been shown to capture signatures of coherent electron tunneling as well as coherent response to the optical field [30–34]. However, such models have not yet been applied to a quantum-dot QC laser where electron-phonon coupling is strong. Moreover, most density matrix methods use a fully derived algebraic solution, which quickly becomes cumbersome when considering more than three to four states. One exception is Ref. [35], which accommodates an arbitrarily large basis, although it stopped short of including coherent optical response. The latter point was accounted for in Ref. [36], in which the coherent gain and transport characteristics were calculated in a proposed silicon-based terahertz QCL.

In this paper, we present a density matrix approach suitable for steady-state modeling of transport and optical properties

*bburnett@ucla.edu

in QC systems of arbitrary size. While typical models for QC lasers use a Hilbert space of electronic states only, we apply the concept more generally where the density matrix represents a combined system of electronic (sublevel) and bosonic (LO phonon) degrees of freedom. This allows simultaneous consideration of coherent electron-LO-phonon interaction, electron tunneling, and the optical field, alongside incoherent transition and dephasing mechanisms. A nanopillar geometry is used as a model for quantum confinement, although our treatment is generally applicable to any cascaded quantum dot based structure. Results predict a complicated multipeaked gain spectrum, and highlight the importance of dephasing on both transport and gain characteristics. Overall, quantum dot QC lasers will exhibit transport and gain features that are qualitatively different from conventional QC lasers.

II. METHOD

A. Steady-state solution

The unit cell of a QC system is a multiwell module, which contains a finite number of states. The module is repeated a large number of times with a successive energy difference imposed by the electrical bias, as conceptually illustrated in Fig. 1. These states might represent subbands such as in a conventional QC laser, discrete sublevels as in a quantum-dot system, or even product states of a combined system such as the electron/LO-phonon tensor product Hilbert space used in this work. The states are coupled together by a variety of coherent processes (such as resonant tunneling, LO-phonon interaction, and optical-field dipole coupling) and incoherent processes (such as acoustic phonon scattering and pure dephasing) that result in charge transport and optical gain. Reflecting this, we will assume that the system Hamiltonian is known, and allow that the time evolution of the representative density matrix (ρ) consists of a coherent Liouville-von Neumann component

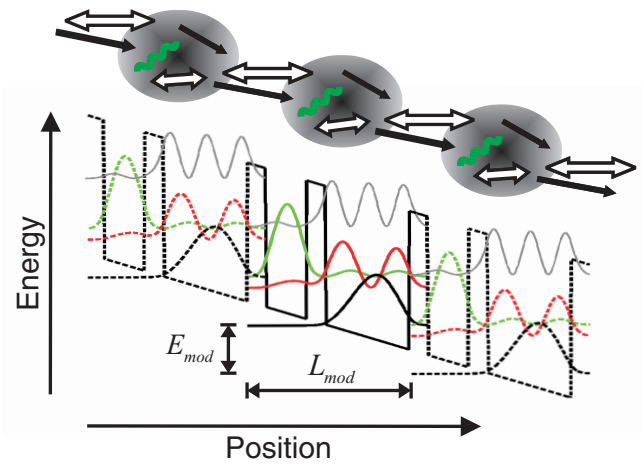

FIG. 1. (Color online) Conceptual schematic of a representative three-level quantum-cascade system, which is periodic in both position and energy. Interactive processes will be incorporated as static couplings (empty double arrows), an optical field (green), and irreversible transition processes (solid single arrows). The lower part depicts an example energy structure, where the black lines are the conduction band profile and the probability densities for each subband/level are shown.

alongside an incoherent component due to transitions and dephasing [37,38]:

$$\frac{d}{dt}\rho = \frac{d}{dt}\rho\Big|^{\text{coh}} + \frac{d}{dt}\rho\Big|^{\text{inc}} = -\frac{i}{\hbar}\mathcal{L}^H\rho + \frac{d}{dt}\rho\Big|^{\text{inc}}. \quad (1)$$

$\mathcal{L}^H \equiv [H,\dots]$ is known as the Liouville superoperator. Through its tetradic form, it can be understood as relating the elements of ρ to the coherent part of its own time evolution, where

$$\frac{d}{dt}\rho_{ab}\Big|^{\text{coh}} = -\frac{i}{\hbar}\sum_{cd}\mathcal{L}^H_{abcd}\rho_{cd} = -\frac{i}{\hbar}\sum_{cd}\left(\delta_{bd}H_{ac} - \delta_{ac}H_{db}\right)\rho_{cd}. \quad (2)$$

The periodicity of the cascaded modules allows us to express H and ρ in block matrix form as

$$H = \begin{bmatrix} \ddots & \vdots & & \iddots \\ & (H_0-\Delta) & (H_1) & (H_2) & \\ \cdots & (H_{-1}) & (H_0) & (H_1) & \cdots \\ & (H_{-2}) & (H_{-1}) & (H_0+\Delta) & \\ \iddots & \vdots & & \ddots \end{bmatrix}, \quad (3)$$

$$\rho = \begin{bmatrix} \ddots & \vdots & & \iddots \\ & (\rho_0) & (\rho_1) & (\rho_2) & \\ \cdots & (\rho_{-1}) & (\rho_0) & (\rho_1) & \cdots \\ & (\rho_{-2}) & (\rho_{-1}) & (\rho_0) & \\ \iddots & \vdots & & \ddots \end{bmatrix}. \quad (4)$$

Each submatrix depicted in Eqs. (3) and (4) is of size $N \times N$, where N is the number of levels in each repetitive module. H_0 and ρ_0 represent the intramodule Hamiltonian and density matrix, while $H_{\pm p}$ and and $\rho_{\pm p}$ represent the intermodule Hamiltonian and coherences for modules spaced p apart. The matrix $\Delta = E_{\text{mod}}\mathbb{1}_N$ accounts for the applied bias, where E_{mod} is the difference in energy per module. Applying block matrix multiplication in (1) with these matrices, we obtain the equations for the coherent time evolution of all submatrices, which collectively describe the entire system:

$$\frac{d}{dt}\rho_p\Big|^{\text{coh}} = -\frac{i}{\hbar}\left(\sum_q [H_{p-q},\rho_q] - pE_{\text{mod}}\rho_p\right). \quad (5)$$

In order to consider interactions with a harmonic electromagnetic field, we expand at steady-state each submatrix of H and ρ into harmonics of order α at frequency ω:

$$H_p = \sum_\alpha H_p^{(\alpha)}e^{i\alpha\omega t}, \quad \rho_p = \sum_\alpha \rho_p^{(\alpha)}e^{i\alpha\omega t}, \quad (6)$$

where the sums could in principle run over all integers $(-\infty,\infty)$. Substituting (6) into (5), and selecting a particular harmonic m, we obtain with incoherent effects omitted:

$$im\omega\rho_p^{(m)} = -\frac{i}{\hbar}\left(\sum_{q\alpha}\left[H_{p-q}^{(\alpha)},\rho_q^{(m-\alpha)}\right] - p\Delta\rho_p^{(m)}\right). \quad (7)$$

An equation can be obtained at each element in (7) by invoking the Liouville superoperator and a change of variables:

$$im\omega\rho^{(m)}_{p,ab} = -\frac{i}{\hbar}\left(\sum_{qncd}\left(\mathcal{L}^{H^{(m-n)}_{p-q}}_{abcd}\rho^{(n)}_{q,cd}\right) - pE_{\mathrm{mod}}\rho^{(m)}_{p,ab}\right). \quad (8)$$

Terms outside the quadruple sum can then be brought inside using Kronecker δ functions, yielding a system of equations providing the relation $\sum_{qncd} M_{(ab)^n_p,(cd)^n_q}\rho^{(n)}_{q,cd} = 0$, where

$$M_{(ab)^m_p,(cd)^n_q} = -\frac{i}{\hbar}\mathcal{L}^{H^{(m-n)}_{p-q}}_{abcd} + i\delta_{pq}\delta_{mn}\delta_{ac}\delta_{bd}\left(p\frac{E_{\mathrm{mod}}}{\hbar} - m\omega\right) + S_{(ab)^m_p,(cd)^n_q}. \quad (9)$$

The incoherent contribution $S_{(ab)^p_m,(cd)^q_n}$ is addressed in Appendix. Once a population sum condition is substituted at a single row in M, the entire steady-state solution is attainable by the matrix equation $M \times A = B$, where A is a list of the unknowns and B is a matching vector of zeros with the single exception of a 1 in the sum row.

For a module consisting of N states, and considering up to P nearest-module couplings and harmonics up to $e^{\pm iQ\omega t}$, the number of unknowns is $N^2(2P+1)(2Q+1)$. Although the method as formulated can, in principle, accommodate arbitrarily higher N, P, and Q, in this work, we restrict our analysis to only nearest-module coupling and single harmonics, such that the number of unknowns is $9N^2$.

B. Optical gain

Gain is computed through the induced harmonic polarization in response to an optical field $E_{\mathrm{opt}} = |E|e^{i\omega t} + \mathrm{c.c.}$ If the position operator z is known, the harmonic Hamiltonian is then $H^{(\pm1)} = q|E|z$, and the polarization is found using $P = N_d q\langle z\rangle = N_d q\mathrm{Tr}(\rho z)$. We assume that by some choice of basis, z has only diagonal submatrices:

$$z = \begin{bmatrix} \ddots & & \vdots & & \iddots \\ & (z_0-\Delta_z) & 0 & 0 & \\ \cdots & 0 & z_0 & 0 & \cdots \\ & 0 & 0 & (z_0+\Delta_z) & \\ \iddots & & \vdots & & \ddots \end{bmatrix}, \quad (10)$$

where $\Delta_z = L_{\mathrm{mod}}\mathbb{1}_N$ accounts for the spatial separation between modules. Since the population sum is normalized to a single module, the trace over one diagonal submatrix is effectively a trace over the entire problem. Taking only the harmonic component, the optical susceptibility is then

$$\chi_{\mathrm{opt}}(\omega) = \frac{N_d q}{\epsilon_0|E|}\mathrm{Tr}\left(\rho^{(1)}_0 z_0\right), \quad (11)$$

from which the material gain per unit length can be calculated as $g = 2\mathrm{Im}(\sqrt{\epsilon_s + \chi_{\mathrm{opt}}}\omega/c)$, ϵ_s being the background dielectric constant. In this way, the gain material is treated as an effective medium.

By carrying out the trace in (11), it is seen that there are susceptibilities associated with each transition, which add directly:

$$\chi_{\mathrm{opt}}(\omega) = \sum_{\alpha\beta}\chi_{\alpha\beta}(\omega) = \frac{N_d q}{\epsilon_0|E|}\sum_{\alpha\beta}\rho^{(1)}_{\alpha\beta}z_{\beta\alpha}, \quad (12)$$

so that contributions can be examined for different transitions independently.

C. Current

Current is computed from the expectation value of velocity. However, since the time evolution includes both coherent and incoherent components, the velocity will have contributions from both as well:

$$J = N_d q\mathrm{Tr}(\rho v^{\mathrm{coh}}) + J^{\mathrm{inc}}. \quad (13)$$

Using $v^{\mathrm{coh}} = \frac{i}{\hbar}[H,z]$, and assuming that H has the form of (3) with only a single harmonic and z has the form of (10), the static component of current due to coherent velocity is found to be

$$J^{\mathrm{coh}} = \frac{iN_d q}{\hbar}\mathrm{Tr}\sum_p \rho^{(0)}_p\left(\left[H^{(0)}_{-p},z_0\right] - pL_{\mathrm{mod}}H^{(0)}_{-p}\right) + \rho^{(1)}_p\left(\left[H^{(-1)}_{-p},z_0\right] - pL_{\mathrm{mod}}H^{(-1)}_{-p}\right) + \rho^{(-1)}_p\left(\left[H^{(1)}_{-p},z_0\right] - pL_{\mathrm{mod}}H^{(1)}_{-p}\right). \quad (14)$$

The second and third terms are optically induced currents (stimulated emission and absorption). If vanishing optical intensity is assumed, we are left with the expression for coherent current density below threshold:

$$J^{\mathrm{coh}} = \frac{iN_d q}{\hbar}\mathrm{Tr}\sum_p \rho^{(0)}_p\left(\left[H^{(0)}_{-p},z_0\right] - pL_{\mathrm{mod}}H^{(0)}_{-p}\right). \quad (15)$$

The incoherent contribution J^{inc} accounts for the semiclassical "hopping" velocity due to incoherent transitions between spatially localized basis states. It is described in more detail in Appendix.

III. ELECTRON-LO-PHONON COUPLING

Interaction of a discrete electronic density of states with a manifold of nearly degenerate LO-phonon modes is a particularly distinct problem in that dephasing is weakened due to the lack of a continuum of states. In this way, it is similar to an atom strongly coupled to a single optical cavity mode, where higher-order coherent quantum effects become possible and so the electron-boson interaction cannot be treated using Fermi's "golden rule." The simplest example is in a two-state electronic system, where electrons do not relax irreversibly from the higher energy state to the lower one, but rather undergo a sustained Rabi oscillation which continues until interrupted by another process such as the decay of the emitted phonon or interaction of the electron with the outside [17–20,22,23,39,40].

The excitations of a phonon coupled to an electronic transition are quasiparticles known as polarons. However, rather than use the polaron states as our basis, we choose a basis formed by a tensor product of the electronic sublevel Hilbert space with LO-phonon number states; these are then coupled together by the electron-phonon (Fröhlich) Hamiltonian. This

choice is important, as it determines that in the limit of weak dephasing the system will form coherent polarons, but will relax into a separable state as the dephasing becomes strong in comparison to the polaron splitting. In addition, this allows for both electron and phonon distributions to reach a nonequilibrium steady state, and also simplifies the inclusion of electron tunneling, phonon decay and generation, and the optical field. Our particular application allows consideration of coherent polarons comprising multiple phonon modes and multiple electronic intersublevel transitions, each of which may have (in principle) their own dephasing rates. Furthermore, unlike the case of an isolated quantum dot, where decay of the phonon component dominates polaron decay, we can also include decay of the electronic component, through tunneling, or some other incoherent scattering mechanism.

A comparison can be made between our treatment of polaron effects and that employed in the NEGF simulations of Refs. [26–29]. In these works, the electron-phonon interaction is accounted for by a phonon Greens function which enters into the electron self-energy; it is therefore represented as an average field which is assumed to remain at thermal equilibrium. The phonon decay, which broadens the interaction, is treated by introducing an anharmonicity in the phonon Greens function. Our work, on the other hand, treats the electron-phonon interaction in a similar manner to the Jaynes-Cummings model in quantum optics, where the LO phonons themselves become as much a part of the system as the electrons, decaying towards equilibrium by their interaction with acoustic phonons. In this way, it is the acoustic, rather than LO phonons that play the role of the system bath.

A. Single transition

The electron-LO-phonon interaction is described by the Fröhlich Hamiltonian $\hat{H}_f$, which includes all modes simultaneously. Assuming bulk plane-wave LO-phonons with wave vectors $\vec{k}$, $\hat{H}_f = \sum_{\vec{k}} \hat{F}_{\vec{k}}$, where $\hat{F}_{\vec{k}}$ is the Fröhlich Hamiltonian for single mode $\vec{k}$, expressed as

$$\hat{F}_{\vec{k}} = \frac{A}{k\sqrt{V}}(e^{i\vec{k}\cdot\vec{r}} b_{\vec{k}} + e^{-i\vec{k}\cdot\vec{r}} b^{\dagger}_{\vec{k}}), \tag{16}$$

where the constant $A = \sqrt{\frac{E_{\mathrm{LO}} q^2}{2}(\frac{1}{\epsilon_\infty} - \frac{1}{\epsilon_{\mathrm{dc}}})}$. V is the crystal volume, $b_{\vec{k}}$ and $b^{\dagger}_{\vec{k}}$ are annihilation and creation operators, and ϵ_∞ and ϵ_{dc} are the high- and low-frequency bulk permittivities. For a particular transition which involves electronic states ψ_1 and ψ_2, we form product states with LO-phonon modes $\vec{k}$ and define the matrix elements

$$F_{\vec{k},T} \equiv \langle \psi_1; 0|\hat{H}_f|\psi_2; 1_{\vec{k}}\rangle = \langle \psi_1; 0|\hat{F}_{\vec{k}}|\psi_2; 1_{\vec{k}}\rangle. \tag{17}$$

We now follow previous works and introduce a particular LO-phonon mode T, which is a superposition of plane-wave modes, defined through any number state $|n_T\rangle$ [39,40]:

$$|n_T\rangle \equiv \frac{1}{\sqrt{\sum_{\vec{k}} |F_{\vec{k},T}|^2}} \sum_{\vec{k}} F^*_{\vec{k},T} |n_{\vec{k}}\rangle. \tag{18}$$

Under assumption of LO-phonon degeneracy, this mode remains an energy eigenmode. This is valid given that the interaction strength falls off rapidly for phonon wave vectors not much larger than the inverse dot size (∼20 nm), so that the relevant phonon modes comprise only a small part of the Brillouin zone close to the Γ point. The coupling strength to mode T is then

$$\langle \psi_1; 0|\hat{H}_f|\psi_2; 1_T\rangle = \sqrt{\sum_{\vec{k}} |F_{\vec{k},T}|^2} \equiv \Omega_{\mathrm{pol},T}, \tag{19}$$

while it can be shown that the matrix element involving any orthogonal mode is zero. Therefore the problem reduces to one involving only a single mode.

In the form of an integral over $\vec{k}$, the expression for $\Omega_{\mathrm{pol},T}$ becomes

$$\Omega_{\mathrm{pol},T} = \frac{A^2}{(2\pi)^3} \int_{\vec{k}} d^3\vec{k} |\mathcal{F}^{(T)}(\vec{k})|^2/k^2, \tag{20}$$

where we have defined the form-factor for the transition

$$\mathcal{F}^{(T)}(\vec{k}) \equiv \langle \psi_1 | e^{i\vec{k}\cdot\vec{r}} | \psi_2 \rangle. \tag{21}$$

The displacement field for such a mode can be constructed using (18). To obtain a more physical understanding of this mode, we consider the lowest energy intersublevel transition in a simple cylindrical quantum dot with a height of 30 nm and a diameter of 20 nm, with an infinite confinement potential on all sides. The wave functions are thus products of the infinite square well ground and first excited states in the axial direction with the circular well ground state in the cross-sectional plane. A plot of upward and radial displacements for the associated phonon mode are depicted in Fig. 2. This helps to justify our use of an unbounded plane wave basis—the results are not very different than if confined modes were used.

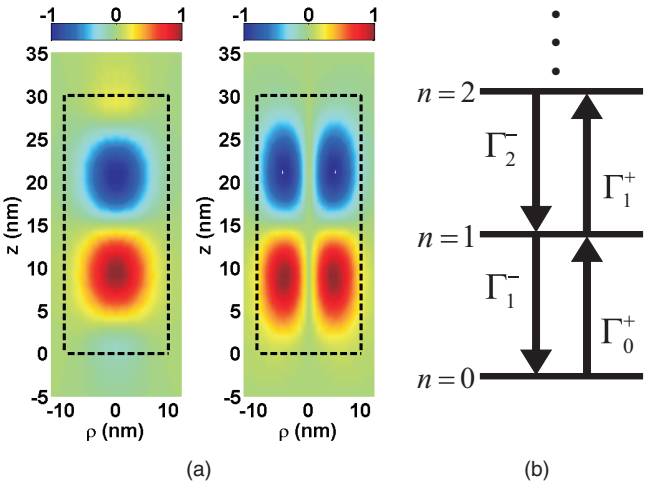

FIG. 2. (Color online) (a) The particular phonon mode interacting with a cylindrical QD lowest-lying transition: (left) upward and (right) radial displacements. Both are in separate arbitrary units. Dashed lines denote the dot boundary ($h = 30$ nm, d= 20 nm). Red and blue areas are maxima opposite in sign, and the radial displacement is shown at a phase $\pi/2$ relative to that of the upward. (b) Generation and decay processes represented as transitions between number states of a single phonon mode.

B. Extension to two transitions

We next consider a system with two intersublevel transitions, both of which interact coherently with LO phonons. These will later be identified as the nonradiative depopulation ($\psi_L \rightarrow \psi_I$) and radiative lasing ($\psi_U \rightarrow \psi_L$) transitions, respectively.

In considering more than one transition, it is found that we can define a particular mode associated with each. However, the problem arises that these modes are not generally the same nor orthogonal to one another. The transitions of our concern would couple to phonon modes N and R, respectively, but we can choose instead basis modes N and α, where α is a mode in the NR plane of the mode space, but orthogonal to N. This amounts to an orthonormalization within the basis of modes N and R, which could be performed on a larger number of modes using a Gram-Schmidt process.

The matrix element for any electronic transition coupling to any arbitrary phonon mode Q is

$$\langle \psi_1; 0|\hat{H}_f|\psi_2; 1_Q\rangle = \Omega_{\mathrm{pol},T}\langle T\cdot Q\rangle, \tag{22}$$

where $\langle T\cdot Q\rangle$ is the normalized inner product of mode Q with the mode associated with the transition. Therefore the important matrix elements governing the problem when considering phonon modes N and α are given for the N transition as

$$\begin{aligned}\langle \psi_L; 0|\hat{H}_f|\psi_I; 1_N\rangle &= \Omega_{\mathrm{pol},N},\\ \langle \psi_L; 0|\hat{H}_f|\psi_I; 1_\alpha\rangle &= 0,\end{aligned} \tag{23}$$

and for the R transition as

$$\begin{aligned}\langle \psi_U; 0|\hat{H}_f|\psi_L; 1_N\rangle &= \Omega_{\mathrm{pol},R}\langle R\cdot N\rangle,\\ \langle \psi_U; 0|\hat{H}_f|\psi_L; 1_\alpha\rangle &= \Omega_{\mathrm{pol},R}\langle R\cdot \alpha\rangle.\end{aligned} \tag{24}$$

The inner product $\langle R\cdot N\rangle$ can be computed by a sum over phonon modes as

$$\langle R\cdot N\rangle = \frac{1}{\Omega_{\mathrm{pol},R}\Omega_{\mathrm{pol},N}}\sum_{\vec{k}} F_{\vec{k},R}F^*_{\vec{k},N}, \tag{25}$$

or as an integral by

$$\langle R\cdot N\rangle = \frac{A^2}{(2\pi)^3}\frac{1}{\Omega_{\mathrm{pol},R}\Omega_{\mathrm{pol},N}}\int_{\vec{k}} d^3\vec{k}\,\mathcal{F}^{(N)*}(\vec{k})\mathcal{F}^{(R)}(\vec{k})/k^2. \tag{26}$$

For simplicity, we choose an overall phase for α such that $\langle R\cdot\alpha\rangle$ is positive real. Then, since α lies in the plane defined by R and N, we have that

$$\langle R\cdot\alpha\rangle = \sqrt{1-|\langle R\cdot N\rangle|^2}. \tag{27}$$

C. Phonon decay and generation

LO phonons have a finite lifetime due to anharmonic decay, typically into pairs of acoustic phonons [41]. A rigorous computation of the relaxation time τ_r for the LO-phonon distribution towards equilibrium in spherical quantum dots was performed by Li and Arakawa [42]. It was found to be only weakly size-dependent for GaAs dots of diameters greater than 15 nm, and results were nearly identical for the two modes considered. In our model, we use the approximate fit to their results for all modes:

$$\tau_r(T) = \left[8 - \frac{T}{54.5\ \mathrm{K}}\right]\mathrm{ps}. \tag{28}$$

τ_r involves both the competing decay and generation processes, where by detailed balance the two are equal and opposite at thermal equilibrium. Specifically, it is defined as

$$\frac{1}{\tau_r} \equiv -\frac{\Gamma^+ - \Gamma^-}{\delta N}, \tag{29}$$

where $\Gamma^\pm$ are the generation and decay rates and δN is the deviation from equilibrium. We are interested in the bare decay and generation rates $\Gamma^\pm_n$, which are the transition rates between number states n as depicted in Fig. 2(b). From the form of the interaction Hamiltonian governing the LO-phonon decay [42–44], it is found that $\Gamma^+_n = (n+1)\Gamma^+_0$ and that $\Gamma^-_n = n\Gamma^-_1$. Combining this result with (29) and enforcing thermodynamic equilibrium, the decay and generation rates can be expressed in terms of the relaxation rate as

$$\begin{aligned}\Gamma^-_n &= \frac{1}{\tau_r}\frac{n}{1-e^{-E_{\mathrm{LO}}/k_BT}},\\ \Gamma^+_n &= \frac{1}{\tau_r}\frac{n+1}{e^{E_{\mathrm{LO}}/k_BT}-1} = \frac{1}{\tau_r}(n+1)n_{\mathrm{LO}},\end{aligned} \tag{30}$$

where n_{LO} is the Bose-Einstein factor evaluated at the LO-phonon energy. At low temperature, the generation is extremely slow such that relaxation is dominated by the decay, but at temperatures approaching 300 K, the generation does become significant.

IV. APPLICATION

We are now in the position to compute the steady-state transport and gain characteristics of a model quantum dot QC laser. We choose perhaps the simplest possible system—a two dot module containing three electronic states. We treat the lateral quantum confinement as an infinite cylindrical potential, which allows separation of variables between the axial and lateral dimensions. This could approximate for example the confinement of etched nanopillars [13,14], or nanowires grown with a core-shell heterostructure [45,46]. In order to keep the problem tractable, we only consider the case where the lateral quantum confinement is sufficient so that only the lowest lateral energy state is relevant. In practice, this would require lateral confinement which is strong enough that the s-p energy separation is significantly above E_{LO}. In GaAs and approximating the lateral confinement as circular, we obtain a value of 50 meV for the energy separation in a confinement diameter of 20 nm.

A. Model system

The band structure in the growth direction for our model system in GaAs/$Al_{0.2}Ga_{0.8}As$, adapted from Refs. [47,48], is shown in Fig. 3. The design features a tunnel injection, followed by a diagonal radiative transition, and resonant phonon depopulation. The diagonality is intended to reduce the strength of the phonon interaction with the lasing transition. Fully discrete electronic states are formed by products of the pictured axial states with the infinite circular well ground

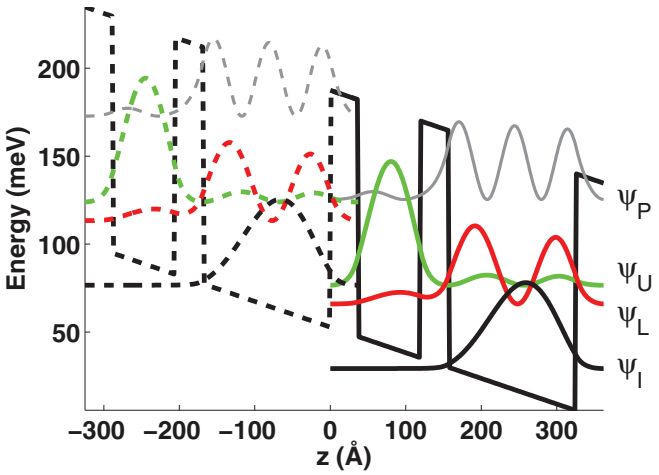

FIG. 3. (Color online) Band structure in the growth direction for the model system, computed from a two-well tight-binding standpoint. The layer thicknesses in angstroms starting from the injector barrier are 37/82/38/168. The lasing transition at injection anticrossing is 10.6 meV (2.56 THz), the phonon depopulation transition is 36.7 meV, and the injection anticrossing gap is 3.8 meV. The dipole matrix element for the optical transition is 4.7 nm.

(s) state in the lateral directions: $\psi(z,\rho,\theta) = \psi_z(z)J_0(k_\parallel \rho)$, where ψ_z is the axial wave function, J_0 is the zero order Bessel function, and $k_\parallel$ is an in-plane wave vector, which matches the pillar wall boundary condition at the first Bessel zero. A diagram of the relevant tunneling and electron-phonon interactions is given in Fig. 4. To begin, tunneling will be considered only through the intended channel between the injector and upper radiative states; a parasitic tunneling mechanism coupling the injector to the lower radiative state

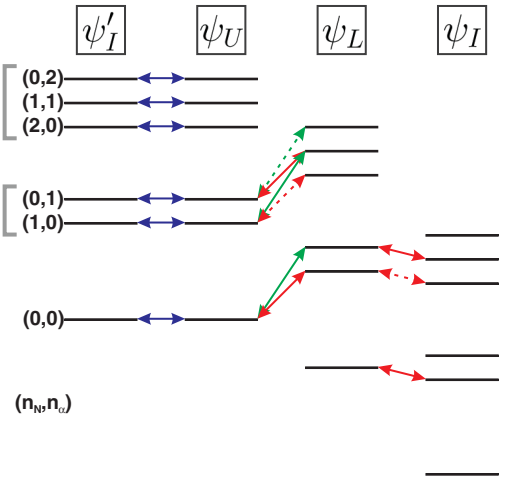

FIG. 4. (Color online) Relevant tunneling and electron-phonon interactions. Arrows represent: red is a coupling with N phonons, green is a coupling with α phonons, and blue are the tunneling processes. Not shown is a parasitic tunnel coupling between ψ_I' and ψ_L, which will be neglected until Sec. IV F. The vertical axis represents energy, although states grouped together are degenerate. Dashed arrows represent couplings between phonon numbers 1 and 2, which have a strength of $\sqrt{2}$ times those between 0 and 1. The module boundary is defined at the tunnel coupling, between the injector and upper electronic states.

will be accounted for and studied in Sec. IV F. We find that the most important of the electron-phonon couplings occur across the depopulation ($\psi_L \rightarrow \psi_I$) transition and the radiative ($\psi_U \rightarrow \psi_L$) transition.

At design biases, we can safely neglect coupling to the higher energy parasitic state ψ_P, and so it is not considered as part of our calculation. Basis states for the combined electron-phonon system are constructed as tensor products of the three electronic states ψ_I, ψ_L, and ψ_U with phonon number states in modes N and α, where these modes are defined in the manner described in the previous section. We allow the total number of phonons in both modes to reach up to two, and the decay and generation rates pertaining to both are assumed to follow the results from Ref. [42] and the previous section. The optical Hamiltonian is constructed from the dipole operator z_0, which is expanded appropriately into the tensor product basis.

It must be noted that each module in reality contains its own pair of phonon modes N and α, and so by constructing our schematic of interactions as shown in Fig. 4, we are implicitly enforcing that the occupations in all modules are perfectly correlated. This is of course not the case in a real system; however, this approximation is necessary in order to make the problem tractable. With faster dephasing, coherences spanning the entire module are reduced, making the approximation closer to exact.

The values relevant to the electron-phonon interaction were computed as $\Omega_{\text{pol},R} = 2.5$ meV, $\Omega_{\text{pol},N} = 3.3$ meV, and $\langle R \cdot N \rangle = 0.176$. These calculations were greatly simplified by the assumption of a cylindrical cross-section.

B. Results

A critical parameter is the pure dephasing time T_2^*, which encompasses all processes that decohere the various interactions without changing level populations. It contributes to the linewidth broadening for various transitions (for example, for a two level system, the transition linewidth is increased by $2\hbar/T_2^*$), and also determines the coherence of the various interactions (for example, between states tunnel coupled by Ω if $\hbar/T_2^* \gg \Omega$, the interaction will be incoherent, whereas if $\hbar/T_2^* \ll \Omega$, it will be coherent, exhibiting strong coupling where the two states form an anticrossed doublet).

Theoretical and experimental works suggest that decoherence in quantum dots occurs primarily due to both real and virtual acoustic phonon processes [49,50]. In Ref. [49], T_2^* was measured in InAs self-assembled quantum dots via four-wave mixing; values ranged from 90 ps at 10 K to 9 ps at 120 K. Dephasing was observed to be strongly temperature dependent (more so than the sublevel lifetimes) but also connected to the detailed energy structure of the system. As expected however, these times are much longer than in conventional quantum-well QC lasers, where $T_2^* \sim 300$ fs [31,51]. To simplify this intricate problem, we use a single phenomenological T_2^* parameter throughout our simulations. Unless otherwise specified, we assume $T_2^* = 5$ ps at 300 K, which is a reasonably conservative value and consistent with the computed values of Ref. [50].

Results for the steady-state gain profile and population inversion at 100 and 300 K are shown in Fig. 5 for vanishing optical intensity. The electron density was taken to be

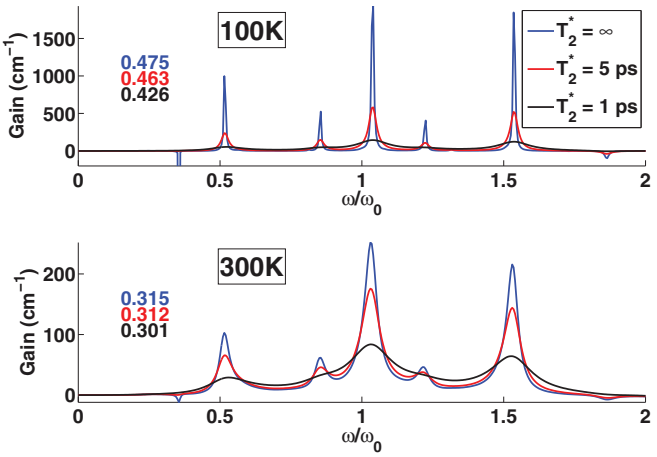

FIG. 5. (Color online) Computed gain profiles at the injection anticrossing bias for pure dephasing times T_2^* of 1 ps, 5 ps, and ∞ at 100 and 300 K, with vanishing optical intensity. Colored numbers on the left give the inverted population fractions.

$N_d = 10^{16}$ cm^{-3}, which corresponds to an active medium made up of a nanopillar array spaced on an 80 nm grid and doped with one electron per well. Pure dephasing times T_2^* of 1 ps, 5 ps, and ∞ were applied to all coherences. T_2^* is especially crucial for the peak gain and linewidth at low temperature, where the lifetimes of the $(n_N,n_\alpha) = (0,0)$ states are extremely long due to the slow generation rate. At both temperatures, it is also noted that reduction in peak gain due to dephasing is attributed mainly to broadening rather than actual loss of population inversion.

Figure 6 shows gain profiles computed from each phonon occupation state separately at a temperature of 300 K and without pure dephasing for clarity. Even at 300 K, the large majority of the gain comes from the (0,0) states, which justifies our truncation at a total of two phonons. This is due to both their larger populations and longer lifetimes resulting in narrower linewidths. By separating the gain into occupation numbers we also note that while the total gain appears to exhibit five peaks, there are in fact more as well as resonance shifts which occur in the higher phonon occupation states.

C. Tunnel coupling dependence

The exact locations of the resonance peaks exhibit a complicated dependence on the coupling parameters and energy

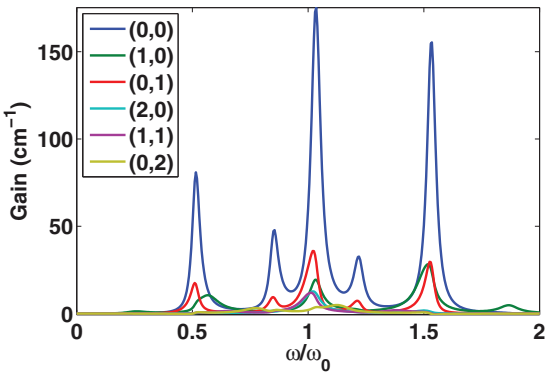

FIG. 6. (Color online) Gain profile separated into phonon occupations for $T = 300$ K and $T_2^* = \infty$.

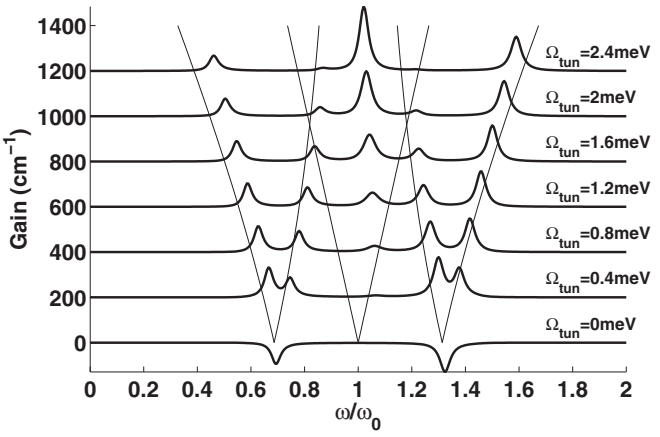

FIG. 7. Zero-phonon gain at 300 K and $T_2^* = \infty$ as the tunnel coupling is turned on. Curves are offset by 200 cm^{-1} for clarity. Thin lines denote the anticipated resonances based on diagonalization of the Hamiltonian for the subspace around the zero-phonon radiative transition not including the phonon coupling across the radiative transition. These energies are given by $E_{\rm rad} \pm \Omega_{\rm tun} \pm \sqrt{\Omega_{\rm tun}^2 + \Omega_{{\rm pol},N}^2}$ and $E_{\rm rad} \pm \Omega_{\rm tun}$.

structure due to the complex nature of the chain-coupled problem, and also experience other shifts due to the damping mechanisms. In Fig. 7, we provide some insight by examining the evolution of the zero-phonon gain profile without pure dephasing as the injection tunnel coupling (one half of the anticrossing gap) is turned on. In practice, this is equivalent to varying the thickness of the injection barrier.

The peak locations can be partially interpreted by diagonalizing H only within the subspaces of states directly coupled to the zero-phonon radiative states, ignoring the phonon coupling across the radiative transition itself. The upper radiative state is split into a doublet by the tunnel coupling back to the injector, while the lower radiative state is split into a triplet by the phonon coupling to the next injector followed by the tunnel coupling to the next radiative state. This model is sufficient at low tunnel coupling, where at $\Omega_{\rm tun} = 0$ only the polaronic splitting exists, and the peak at the central frequency is absent due to its vanishing coupling strength to radiation. As the tunnel coupling strength is increased, the peak near center frequency begins to emerge and eventually dominates the gain profile. We attribute the emergence of this peak to the onset of the phonon coupling across the radiative transition, which highly expands the Hilbert space relevant even to only the zero-phonon gain. This polaronic splitting represents a major difference compared to a conventional quantum-well QC laser, and must be properly accounted for in any design.

D. Current versus voltage characteristic

Figure 8 shows the transport characteristic at 100 and 300 K, alongside the gain profiles at 300 K for various bias points. The current is significantly higher at 300 K due to the faster phonon decay which results in overall faster transport. The profiles demonstrate noticeable shifts in peak position and amplitude as the voltage is tuned, varying the alignment of the injector states. While this highlights the complexity of the

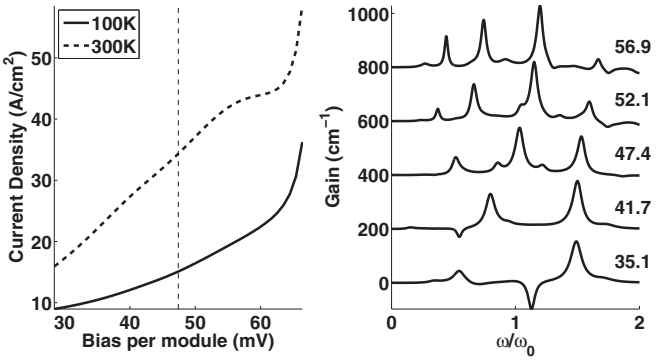

FIG. 8. (Left) Transport characteristic for $T_2^* = 5$ ps. The anticrossing bias is marked by the dashed vertical line. (Right) Gain profile at 300 K for various bias points, labeled by bias/module in millivolts (offset for clarity).

problem, it also suggests that such a device may be a candidate for wide bias-tunability.

A noticeable feature absent from Fig. 8 is the negative differential resistance (NDR) anticipated for biases above the injection resonance (design) bias. This is explained by the phonon bottleneck effect itself, which suppresses transport through the device but is eased by increasing bias as the radiative transition is tuned closer to E_{LO}. In Fig. 9, it is shown that the NDR does in fact emerge if an additional scattering mechanism is included across the radiative transition. The scatterer is considered to be a spontaneous boson emission rate τ_{sp}, which is accompanied by stimulated emission and absorption rates $\tau_{\mathrm{st}} = \tau_{\mathrm{abs}} = \tau_{\mathrm{sp}}/n_r$, where n_r is the Bose-Einstein occupation at the radiative energy. In an actual device, this might represent acoustic phonon scattering, for example. While for a rate $\tau_{\mathrm{sp}} = 100$ ps, a very large increase is seen in the current, the gain remains relatively unaffected for $\tau_{\mathrm{sp}} > 10$ ps.

E. Gain saturation

A particular advantage to our method is the ability to automatically account for effects of increasing optical intensity directly onto the gain profile, allowing us to study gain saturation without needing to extract a stimulated emission rate.

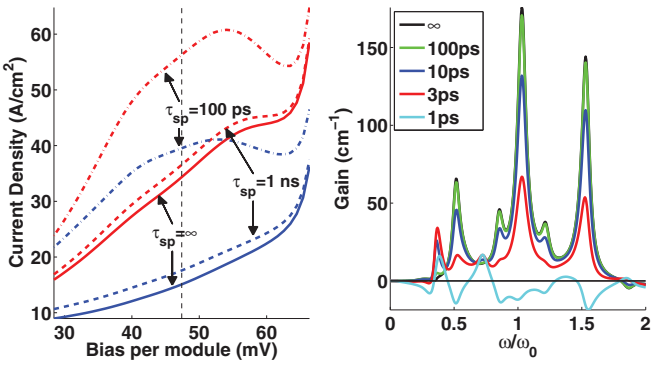

FIG. 9. (Color online) (Left) Transport characteristic as a scattering mechanism is introduced, for $T_2^* = 5$ ps. Blue denotes 100 K and red 300 K. Rates τ_{sp} are ∞, 1 ns, and 100 ps in order of increasing current. (Right) Gain at anticrossing bias, 300 K, for various scattering times τ_{sp}.

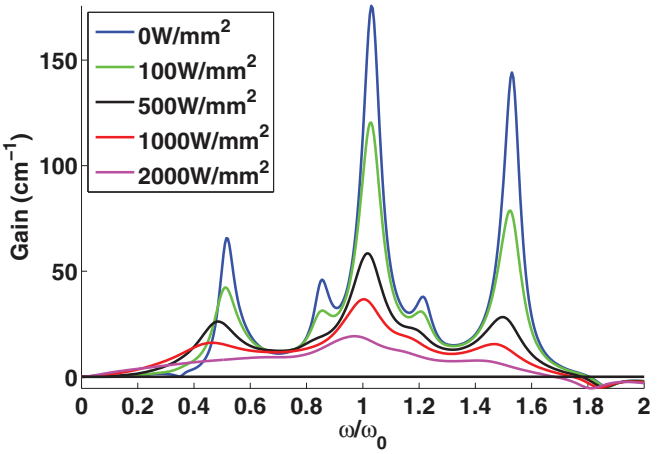

FIG. 10. (Color online) Gain saturation as optical intensity is increased, for $T = 300$ K and $T_2^* = 5$ ps.

Figure 10 shows the change in gain profile as the circulating optical intensity is increased ($I = 2\epsilon_0 nc|E|^2$). Reduction in peak gain is evident due to loss of overall population inversion, redistribution of population among various states, and effective lifetime broadening. In this way, the steady-state optical intensity could be estimated in a laser system by clamping the peak gain to the total cavity losses.

F. Parasitic tunneling

To this point, we have focused on somewhat of an ideal case, where only tunnel coupling from the injector to upper radiative state is considered. However, it is well known that a major issue for THz QC lasers is the existence of a parasitic current channel that occurs for voltage biases below the injection resonance [5,31,52]. While the details vary between designs, this current channel is associated with tunnel coupling from the injector to the lower radiative state or the excited state in the wide depopulation well. The presence of this parasitic current sets a floor on the threshold current density, and if it is too strong, creates a premature NDR, which prevents reaching the design bias. In conventional QC lasers, since this coupling is typically $\Omega_p \sim 0.2$–0.5 meV, the relatively fast dephasing ($T_2^* \sim 0.3$ ps) helps to suppress this current. Since the dephasing times in a quantum dot QC laser are expected to be 1–2 orders of magnitude longer, a concern naturally arises that this parasitic channel will be too strong.

To account for this effect, we now introduce a tunnel coupling from the injector to the lower radiative state, having a value computed from the level anticrossing as $\Omega_p = 0.875$ meV. Although this channel is well detuned at the injection resonance, it is, however, important at lower bias. Figure 11 demonstrates the effect of the parasitic coupling on the transport characteristic for $T_2^* = 5$ ps and 1 ps, and the gain at various bias points for $T_2^* = 5$ ps. Very large current flow is found at biases over a wide range around the parasitic resonance, leading to a considerable NDR. As expected, the gain is significantly modified at lower bias points while at higher bias the parasitic tunneling becomes unimportant as it is further detuned.

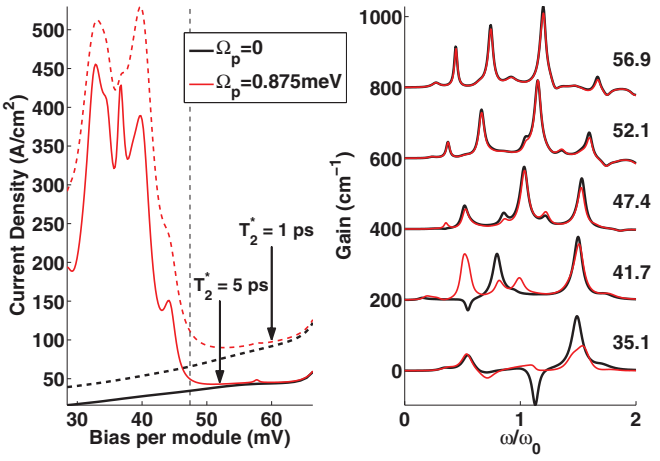

FIG. 11. (Color online) Effects of a parasitic tunneling channel at $T = 300$ K. (Left) Modified transport characteristic for $T_2^* = 5$ and 1 ps. (Right) Modified gain at various bias points for $T_2^* = 5$ ps (labelled in mV/module and offset by 200 cm^{-1} for clarity).

A similar current instability was predicted in Ref. [28], where the possibility of doubling all barrier thicknesses was explored. In our two-well design, where the radiative transition is diagonal, it is clearly disadvantageous to increase the radiative barrier, but, for example, doubling only the injector barrier thickness from 3.7 to 7.4 nm reduces the injection coupling from 1.9 to 0.3 meV and the parasitic coupling from 0.875 to 0.2 meV. However, this reduction in the injection coupling introduces other complications, importantly a large splitting in the gain spectrum as shown in Fig. 7. Furthermore, in order to appreciably reduce the parasitic current level, one requires the coupling to be $\Omega_p \ll \hbar/T_2^*$ (0.13 meV for $T_2^* = 5$ ps), which is difficult to achieve in this simple two-well design. It is likely that more sophisticated designs will be required that selectively reduce the parasitic tunnel coupling, although this will be at the cost of device and material complexity.

V. CONCLUSIONS

A density matrix formulation has been derived for computing the steady-state gain and current in quantum cascade systems of arbitrary size driven by a classical light field. Gain is calculated coherently from the optical susceptibility which arises from the induced harmonic coherences. The method is also useful for other quantum-cascade systems, and could readily be generalized for the study of nonlinear effects such as harmonic, sum frequency, and difference frequency generation.

The method was applied to a nanopillar-based quantum dot QC laser, where coherent interaction of the discrete electronic density of states with quantized LO-phonon modes was accounted for alongside phonon decay processes, electron tunneling, and the light field. Results predict a complex dependence on coupling parameters, energy structure, and damping parameters, and forecast high temperature operation, wide bias tunability, and considerable robustness to added scattering mechanisms. A simple way to account for gain saturation was demonstrated, and finally the effect of parasitic tunnel coupling was isolated, leading to predictions of possible electrical instability.

This work addresses the feasibility of an idealized quantum dot QC laser, where certain practical concerns such as dot inhomogeneity or interface roughness are not accounted for. A further limitation is the inclusion of only two phonon-coupled transitions, restricting our treatment to the regime of small pillar diameter (∼20 nm in GaAs). As the pillar diameter becomes wider, the higher lateral (p) states become important, thus greatly expanding the necessary Hilbert space and coupling parameters. Such a problem is tractable by this method, although it would require an algorithm for automatically enumerating the basis states and computing matrix elements.

Even in this idealized system, several key conclusions emerge. First, as expected, the formation of intersublevel-LO-phonon polarons is beneficial in the long upper state relaxation times, which leads to significant population inversion levels even at room temperature. This leads to peak gain on the order of 100 cm^{-1} at 300 K, which is sufficient for lasing in a low-loss metal-metal waveguide where the losses are ∼15–30 cm^{-1} [53]. The exact peak values depend upon the pure dephasing parameters, which will require further experimental and theoretical consideration. Second, the coherent polaron formation also leads to a series of level splittings on the order of several meV. This produces a complicated gain spectrum with multiple peaks that depend strongly on bias, the electron-phonon interaction strength, and the tunnel coupling. Third, in our model system the longer dephasing times of several ps lead to a strong parasitic current channel which may cause electrical instabilities. While the simple two-well design presented here has few degrees of freedom, it is possible that new design strategies could minimize this effect.

In summary, future quantum dot QC lasers are predicted to have sufficient gain for room-temperature operation. However, they are likely to encounter fundamentally new transport physics not present in conventional QC lasers, which must be properly accounted for during the design and modeling process. Our results suggest that naively scaling existing terahertz QC-laser designs to the quantum dot limit may meet some difficulty.

ACKNOWLEDGMENTS

This work was partially supported by NSF grants ECCS-1002387 and ECCS-1202591. The authors thank A. Pan for helpful discussions.

APPENDIX: DERIVATION OF INCOHERENT CONTRIBUTION TO M

The incoherent evolution is separated into that due to each transition and pure dephasing:

$$\left.\frac{d}{dt}\rho\right|^{\text{inc}} = \sum_X L^X\rho + D\rho. \tag{A1}$$

L^X is the Lindblad superoperator for transition X, which is constructed in the form [38,54]

$$L^X\rho = C^X\rho C^{X\dagger} - \tfrac{1}{2}(C^{X\dagger}C^X\rho + \rho C^{X\dagger}C^X), \tag{A2}$$

where C^X is the jump operator which induces the transition. For a simple transition $\psi_i \to \psi_f$ having rate $\Gamma_{i\to f}$, the

associated jump operator is $C = \sqrt{\Gamma_{i\to f}}|\psi_f\rangle\langle\psi_i|$. In this case, C will have only one nonzero element, but in a combined Hilbert space this may not be true; C itself must be expanded as a tensor product and thus can acquire more than one nonzero element, in which case transfers of coherence can occur.

For example, we can examine the collapse operator which is due to the transition of phonon mode N from $n_N = 1$ to $n_N = 0$. Given the allowed mode occupations, the collapse operator in the space of $\{|n_N, n_\alpha\rangle\}$ is then $C^{1_N\to 0_N} = \sqrt{\Gamma_1^-}\,(|00\rangle\langle 10| + |01\rangle\langle 11|)$. If $N_{\rm el}$ electron degrees of freedom are included, $C^{1_N\to 0_N}$ is further expanded to $\sqrt{\Gamma_1^-}\mathbb{1}_{N_{\rm el}} \otimes (|00\rangle\langle 10| + |01\rangle\langle 11|)$. We will neglect correlations in the different transition processes between number states of a given phonon mode by including separate jump operators for each.

Once the jump operators are obtained, we need to use them to fill out elements of $S_{(ab)_p^m,(cd)_q^n}$ in the chain-coupled system. These are defined as

$$[L^X\rho]^{(m)}_{p,ab} \equiv \sum_{qncd} S^X_{(ab)_p^m,(cd)_q^n}\rho^{(n)}_{q,cd}, \tag{A3}$$

or in other words the coefficients relating variable $\rho^{(n)}_{q,cd}$ to the evolution of $\rho^{(m)}_{p,ab}$ due to transition X. Importantly, we first distinguish between transitions which are correlated between modules and those that are not. In the former, the jump operator itself assumes a chain-coupled form which forms a single Lindblad superoperator [shown in Eq. (A4)], whereas in the latter there exists a series of jump operators which form separate Lindblad superoperators, which are then superimposed [shown in Eq. (A5)]:

$$L\left(\begin{bmatrix} \ddots & & & \\ & (\bar{C}) & & \\ & & (\bar{C}) & \\ & & & \ddots \end{bmatrix}\right) \tag{A4}$$

$$\cdots + L\left(\begin{bmatrix} \ddots & & & \\ & (\bar{C}) & & \\ & & (0) & \\ & & & \ddots \end{bmatrix}\right) + L\left(\begin{bmatrix} \ddots & & & \\ & (0) & & \\ & & (\bar{C}) & \\ & & & \ddots \end{bmatrix}\right) + \ldots. \tag{A5}$$

In the first case, we find that the elements in S^X are

$$S^X_{(ab)_p^m,(cd)_q^n} = \delta_{pq}\delta_{mn}\big[\bar{C}_{ac}\bar{C}^\dagger_{db} - \tfrac{1}{2}(\delta_{bd}[\bar{C}^\dagger\bar{C}]_{ac} + \delta_{ac}[\bar{C}^\dagger\bar{C}]_{db})\big], \tag{A6}$$

assuming that $\bar{C}$ resides in the diagonal submatrices, and for the second we find that

$$S^X_{(ab)_p^m,(cd)_q^n} = \delta_{pq}\delta_{mn}\big[\delta_{p0}\bar{C}_{ac}\bar{C}^\dagger_{db} - \tfrac{1}{2}(\delta_{bd}[\bar{C}^\dagger\bar{C}]_{ac} + \delta_{ac}[\bar{C}^\dagger\bar{C}]_{db})\big], \tag{A7}$$

independent of any displacement of $\bar{C}$ from the diagonal. Since the collapse operator $\bar{C}$ is always positive, we notice in the solution for S^X that correlated transitions can transfer intermodule coherence while uncorrelated transitions do not.

The pure dephasing contribution D is trivial. For a pure dephasing time T_2^* applied to all coherences, it is

$$D_{(ab)_p^m,(cd)_q^n} = -\frac{1}{T_2^*}\delta_{pq}\delta_{mn}\delta_{ac}\delta_{bd}(1-\delta_{p0}\delta_{ab}), \tag{A8}$$

but can also easily be generalized to incorporate different dephasing times.

Finally, we must derive the expression for the incoherent contribution to velocity, and thus $J^{\rm inc}$. We are interested in the expectation value of velocity due to incoherent processes, and so we equate

$$\langle v^{\rm inc}\rangle \equiv \frac{d}{d}{\rm Tr}(\rho z)\Big|^{\rm inc} = {\rm Tr}\Big[\sum_X L^X\rho z + D\rho z\Big]. \tag{A9}$$

By the assumed form of z in (10), we have for both types of transitions that

$${\rm Tr}(L^X\rho z) = {\rm Tr}[L(\bar{C_X})\rho_0 z_0], \tag{A10}$$

although this will only truly hold for transitions that do not cross the module boundary. It is possible, however, to extend so as to include those that do. The pure dephasing part is

$${\rm Tr}(D\rho z) = -\frac{1}{T_2^*}{\rm Tr}\big[\big(\rho_0^{(0)} - {\rm diag}\rho_0^{(0)}\big)z_0\big], \tag{A11}$$

leading to the incoherent contribution to the current: $J^{\rm inc} = N_d q\langle v^{\rm inc}\rangle$.

[1] J. Faist, F. Capasso, D. L. Sivco, C. Sirtori, A. L. Hutchinson, and A. Y. Cho, Science **264**, 553 (1994).

[2] R. Kohler, A. Tredicucci, F. Beltram, H. E. Beere, E. H. Linfield, A. G. Davies, D. A. Ritchie, R. C. Iotti, and F. Rossi, Nature (London) **417**, 156 (2002).

[3] B. S. Williams, Nat. Photon. **1**, 517 (2007).
[4] S. Fathololoumi, E. Dupont, C. W. I. Chan, Z. R. Wasilewski, S. R. Laframboise, D. Ban, A. Matyas, C. Jirauschek, Q. Hu, and H. C. Liu, Opt. Express **20**, 3866 (2012).
[5] Y. Chassagneux *et al.*, IEEE Trans. Terahertz Sci. Tech. **2**, 83 (2012).
[6] I. A. Dimetriev and R. A. Suris, Physica E **40**, 2007 (2008).
[7] A. Wade, G. Fedorov, D. Smirnov, S. Kumar, B. S. Williams, Q. Hu, and J. L. Reno, Nat. Photonics **3**, 41 (2008).
[8] A. Tredicucci, Nat. Mater. **8**, 775 (2009).
[9] S. Anders, L. Rebohle, F. F. Schrey, W. Schrenk, K. Unterrainer, and G. Strasser, Appl. Phys. Lett. **82**, 3862 (2003).
[10] C. H. Fischer, P. Bhattacharya, and P.-C. Yu, Electron. Lett. **39**, 21 (2003).
[11] C. M. Morris, D. Stehr, H. Kim, T.-A. Truong, C. Pryor, P. M. Petroff, and M. S. Sherwin, Nano Lett. **12**, 1115 (2012).
[12] C.-F. Hsu, J.-S. O, P. Zory, and D. Botez, IEEE J. Sel. Top. Quantum Electron. **6**, 491 (2000).
[13] M. I. Amanti, A. Bismuto, A. M. Beck, L. Isa, K. Kumar, E. Reimhult, and J. Faist, Opt. Express **21**, 10917 (2013).
[14] M. Krall, M. Brandstetter, C. Deutsch, H. Detz, A. M. Andrews, W. Schrenk, G. Strasser, and K. Unterrainer, Opt. Express. **22**, 274 (2014).
[15] J. Urayama, T. B. Norris, J. Singh, and P. Bhattacharya, Phys. Rev. Lett. **86**, 4930 (2001).
[16] E. A. Zibik, T. Grange, B. A. Carpenter, N. E. Porter, R. Ferreira, G. Bastard, D. Stehr, S. Winnerl, M. Helm, H. Y. Liu, M. S. Skolnick, and L. R. Wilson, Nat. Mater. **8**, 803 (2009).
[17] T. Inoshita and H. Sakaki, Phys. Rev. B. **56**, R4355 (1997).
[18] K. Kral and Z. Khas, Phys. Rev. B. **57**, R2061 (1998).
[19] S. Hameau, Y. Guldner, O. Verzelen, R. Ferreira, G. Bastard, J. Zeman, A. Lemaitre, and J. M. Gerard, Phys. Rev. Lett. **83**, 4152 (1999).
[20] O. Verzelen, R. Ferreira, and G. Bastard, Phys. Rev. B. **62**, R4809 (2000).
[21] S. Sauvage, P. Boucaud, R. P. S. M. Lobo, F. Bras, G. Fishman, R. Prazeres, F. Glotin, J. M. Ortega, and J.-M. Gerard, Phys. Rev. Lett. **88**, 177402 (2002).
[22] X.-Q. Li, H. Nakayama, and Y. Arakawa, Phys. Rev. B **59**, 5069 (1999).
[23] T. Grange, R. Ferreira, and G. Bastard, Phys. Rev. B. **76**, 241304 (2007).
[24] S.-C. Lee and A. Wacker, Phys. Rev. B **66**, 245314 (2002).
[25] S.-C. Lee, F. Banit, M. Woerner, and A. Wacker, Phys. Rev. B. **73**, 245320 (2006).
[26] N. Vukmirovic, Z. Ikonic, D. Indjin, and P. Harrison, Phys. Rev. B. **76**, 245313 (2007).
[27] N. Vukmirovic, D. Indjin, Z. Ikonic, and P. Harrison, IEEE Photonics Tech. Lett. **20**, 129 (2008).
[28] T. Grange, Appl. Phys. Lett. **105**, 141105 (2014).
[29] T. Grange, Phys. Rev. B **89**, 165310 (2014).
[30] R. F. Kazarinov and R. A. Suris, Sov. Phys. Semicond. **6**, 120 (1973).
[31] H. Callebaut and Q. Hu, J. Appl. Phys. **98**, 104505 (2005).
[32] S. Kumar and Q. Hu, Phys. Rev. B **80**, 245316 (2009).
[33] E. Dupont, S. Fathololoumi, and H. C. Liu, Phys. Rev. B **81**, 205311 (2010).
[34] I. Savic, N. Vukmirovic, Z. Ikonic, D. Indjin, R. W. Kelsall, P. Harrison, and V. Milanovic, Phys. Rev. B. **76**, 165310 (2007).
[35] R. Terazzi and J. Faist, New J. Phys. **12**, 033045 (2010).
[36] T. V. Dinh, A. Valavanis, L. J. M. Lever, Z. Ikonic, and R. W. Kelsall, Phys. Rev. B. **85**, 235427 (2012).
[37] U. Weiss, *Quantum Dissipative Systems* (World Scientific, Hackensack, NJ, 2008).
[38] M. Le Bellac, *Quantum Physics* (Cambridge University Press, New York, NY, 2006).
[39] T. Stauber, R. Zimmermann, and H. Castella, Phys. Rev. B. **62**, 7336 (2000).
[40] S. Hameau, J. N. Isaia, Y. Guldner, E. Deleporte, O. Verzelen, R. Ferreira, G. Bastard, J. Zeman, and J. M. Gerard, Phys. Rev. B. **65**, 085316 (2002).
[41] G. P. Srivastava, *Physics of Phonons* (A. Hilger, New York, NY, 1990).
[42] X.-Q. Li and Y. Arakawa, Phys. Rev. B **57**, 12285 (1998).
[43] P. G. Klemens, Phys. Rev. **148**, 845 (1966).
[44] S. Usher and G. P. Srivastava, Phys. Rev. B **50**, 14179 (1994).
[45] J. N. Shapiro, A. Lin, P. S. Wong, A. Scofield, C. Tu, P. N. Senanayake, and D. L. Huffaker, Appl. Phys. Lett. **97**, 243102 (2010).
[46] J. Johansson and K. A. Dick, Cryst. Eng. Comm. **13**, 7175 (2011).
[47] S. Kumar, C.-W. I. Chan, Q. Hu, and J. L. Reno, Appl. Phys. Lett. **95**, 141110 (2009).
[48] G. Scalari, M. I. Amanti, C. Walther, R. Terazzi, M. Beck, and J. Faist, Opt. Express. **18**, 8043 (2010).
[49] E. A. Zibik *et al.*, Phys. Rev. B. **77**, 041307 (2008).
[50] T. Grange, Phys. Rev. B. **80**, 245310 (2009).
[51] F. Eickemeyer, F. Eickemeyer, K. Reimann, M. Woerner, T. Elsaesser, S. Barbieri, C. Sirtori, G. Strasser, T. Muller, R. Bratschitsch, and K. Unterrainer, Phys. Rev. Lett. **89**, 047402 (2002).
[52] B. S. Williams, H. Callebaut, S. Kumar, Q. Hu, and J. L. Reno, Appl. Phys. Lett. **82**, 1015 (2003).
[53] M. A. Belkin, J. A. Fan, S. Hormoz, F. Capasso, S. P. Khanna, M. Lachab, A. G. Davies, and E. H. Linfield, Opt. Express **16**, 3242 (2008).
[54] G. Lindblad, Comm. Math. Phys. **48**, 119 (1976).